Topological robustness of classical and quantum optical skyrmions in atmospheric turbulence
Supplementary Material

Zhenyu Guo,[1,*] Cade Peters,[2,*] Nilo Mata-Cervera,[1] Anton Vetlugin,[1]
Ruixiang Guo,[1] Pei Zhang,[3,†] Andrew Forbes,[2,‡] and Yijie Shen[1,4,§]

[1] *Centre for Disruptive Photonic Technologies, School of Physical and Mathematical Sciences, Nanyang Technological University, Singapore 637371, Singapore*
[2] *School of Physics, University of the Witwatersrand, Private Bag 3, Wits 2050, South Africa*
[3] *Ministry of Education Key Laboratory for Nonequilibrium Synthesis and Modulation of Condensed Matter Shaanxi Province Key Laboratory of Quantum Information and Quantum Optoelectronic Devices, School of Physics, Xi'an Jiaotong University, Xi'an 710049, China*
[4] *School of Electrical and Electronic Engineering, Nanyang Technological University, Singapore 639798, Singapore*

(Dated: September 5, 2025)

I. TOPOLOGICALLY PROTECTED QUANTUM SKYRMIONS AGAINST TURBULENCE.

It can be demonstrated from equation (6) in the main text that the skyrmion number remains invariant under coordinate transformations. Therefore, to prove the topological robustness of quantum skyrmions against turbulent disturbances, it suffices to show that the influence of turbulence on quantum states can be expressed in terms of coordinate transformations.

After turbulent evolution, the quantum state can be expressed as:

$$\begin{aligned}|\Psi\rangle = \lambda_1 |LG_{l_1}\rangle_A |H\rangle_B + \lambda_2 |LG_{l_1}\rangle_A |V\rangle_B \\ + \lambda_3 |LG_{l_2}\rangle_A |H\rangle_B + \lambda_4 |LG_{l_2}\rangle_A |V\rangle_B,\end{aligned} \tag{S.1}$$

where λ_i represents the normalized complex coefficients. The impact of quantum state evolution on subsequent analysis is primarily manifested in:

$$\begin{aligned}\mu'(r,\phi) &= \frac{\lambda_2 |LG_{l_1}(r)| + \lambda_4 |LG_{l_2}(r)| e^{i(l_2-l_1)\phi}}{\lambda_1 |LG_{l_1}(r)| + \lambda_3 |LG_{l_2}(r)| e^{i(l_2-l_1)\phi}} \\ &= f'(r,\phi) e^{i\Phi'(r,\phi)},\end{aligned} \tag{S.2}$$

where $f'(r,\phi) = |\mu'(r,\phi)|$, $\Phi'(r,\phi) = arg(\mu'(r,\phi))$. Given that the turbulent perturbation terms make direct analytical solutions exceptionally challenging, we instead employ a coordinate transformation approach. Based on the principle of topological invariance, it suffices to construct a conformal transformation satisfying the following equation to simplify the problem.

$$\mu(r_1,\phi_1) = \mu'(r,\phi). \tag{S.3}$$

Considering the mathematical properties of Laguerre-Gaussian beams[1], the following simplification can be adopted:

$$\varepsilon(\mathrm{r}) = \frac{|\mathrm{LG}_{l_2}(\mathrm{r})|}{|\mathrm{LG}_{l_1}(\mathrm{r})|} = \sqrt{\frac{|l_1|!}{|l_2|!}} \left(\frac{\sqrt{2}\mathrm{r}}{\omega_0}\right)^{|l_2|-|l_1|}, \tag{S.4}$$

where ω_0 represents the beam waist. The solution can be obtained through coordinate transformation as follows:

$$\begin{aligned}r_1 &= \frac{\omega_0}{\sqrt{2}} \cdot \left[\sqrt{\frac{|l_2|!}{|l_1|!}} \cdot \left(\frac{\lambda_1}{\lambda_2} \cdot \left|\frac{\lambda_2 + \lambda_4 \varepsilon(r) e^{i(l_2-l_1)\phi}}{\lambda_1 + \lambda_3 \varepsilon(r) e^{i(l_2-l_1)\phi}}\right|\right)^{\frac{1}{|l_2|-|l_1|}}\right] \\ \phi_1 &= \frac{1}{l_2 - l_1} \arg\left(\frac{\lambda_2 + \lambda_4 \varepsilon(r) e^{i(l_2-l_1)\phi}}{\lambda_1 + \lambda_3 \varepsilon(r) e^{i(l_2-l_1)\phi}}\right).\end{aligned} \tag{S.5}$$

The topological invariance of the skyrmion number under coordinate transformations fundamentally underlies the intrinsic robustness of quantum skyrmions against turbulent perturbations.

II. QUANTUM STATE TOMOGRAPHY

To accurately obtain complete information about the quantum state, we employed a maximum likelihood estimation-based quantum state tomography technique in our experimental research[2]. According to the fundamental principles of quantum information theory, any density matrix satisfying the conditions of being Hermitian, non-negative, and unit-trace can be uniquely expressed in the following form through Cholesky decomposition:

$$\hat{\rho}_{\text{ideal}}(\vec{t}) = \frac{T(\vec{t})^\dagger T(\vec{t})}{\mathrm{Tr}\left\{T(\vec{t})^\dagger T(\vec{t})\right\}}. \tag{S.6}$$

For an n-qubit quantum system, the matrix $T(t)$ is a $2^n \times 2^n$ matrix characterized by 4^n parameters $t =$

* author contributions: These authors contributed equally to the work
† email: zhangpei@mail.ustc.edu.cn
‡ email: andrew.forbes@wits.ac.za
§ email: yijie.shen@ntu.edu.sg

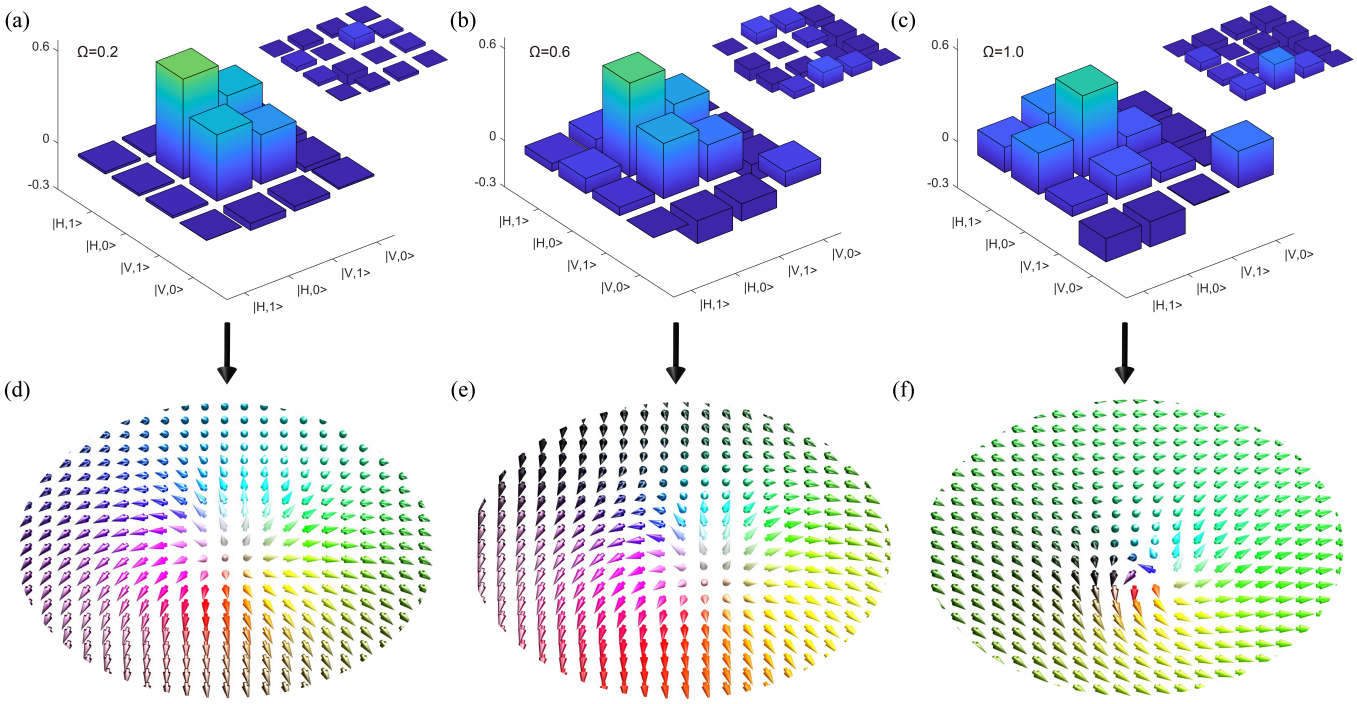

FIG. S1: (a)-(c) present the quantum state tomography reconstruction results of skyrmions under varying turbulence intensities, $\Omega = 2w/r_0$. (d)-(f) corresponding texture structures.

$t_1, t_2, ..., t_{4n}$. Specifically:

$$T(\vec{t}) = \begin{bmatrix} t_1 & 0 & 0 & 0 \\ t_{2^n+1} + it_{2^n+2} & t_2 & 0 & 0 \\ \vdots & & \ddots & \vdots \\ t_{4^n-1} + it_{4^n} & \cdots & t_{2^{n+1}-4} + it_{2^{n+1}-3} & t_{2^n} \end{bmatrix}. \tag{S.7}$$

The crucial next step involves iteratively optimizing the parameter set t based on experimental data n_ν obtained from measurement operators $\hat{\Pi}_\nu$, in order to reconstruct the density matrix estimate that most closely approximates the true quantum state. More precisely, the optimal parameter set t is determined by minimizing the following objective function:

$$\mathcal{L}(\vec{t}) = \frac{1}{2} \sum_{\nu=0}^{4^n-1} \frac{\left[\mathrm{Tr} \left\{ \hat{\Pi}_\nu \hat{\rho}_{\mathrm{ideal}} \left(\vec{t} \right) \right\} - n_\nu \right]^2}{n_\nu}. \tag{S.8}$$

We successfully prepared the quantum skyrmion state in experiments, which can be expressed as:

$$|\Psi\rangle = |0\rangle_A |H\rangle_B + |1\rangle_A |V\rangle_B, \tag{S.9}$$

where $|0\rangle$ and $|1\rangle$ represent the topological charge numbers of OAM, respectively. The experimentally reconstructed density matrices under varying turbulence intensities are presented in Figure S1(a)-(c), exhibiting distinct structural characteristics that correlate with turbulence strength. Upon successfully reconstructing the density matrix ρ through quantum state tomography, we obtain complete statistical information about the quantum state. To quantitatively characterize the entanglement properties of the system, we employ the widely-used entanglement measure for biphoton systems – Concurrence, defined as follows:

$$C(\rho) = \max \left\{ 0, \lambda_1 - \lambda_2 - \lambda_3 - \lambda_4 \right\}, \tag{S.10}$$

where λ_i are the eigenvalues in descending order of the operator $R = \sqrt{\sqrt{\rho}\,\tilde{\rho}\,\sqrt{\rho}}$, with $\tilde{\rho} = (\sigma_y \otimes \sigma_y)\rho^*(\sigma_y \otimes \sigma_y)$, σ_y represent the Pauli-Y operator. The concurrence ranges continuously from 0 for separable states to 1 for maximally entangled states.

Based on the reconstructed density matrix, we can further analyze the spin texture characteristics of quantum skyrmions and calculate their topological charge (skyrmion number). The quantum Stokes parameters can be quantitatively analyzed through the following fundamental expressions:[3]:

$$S_j = \mathrm{Tr} \left(|\bar{r}\rangle_A \langle \bar{r}|_A \otimes \sigma_{B,j} \rho \right) \tag{S.11}$$

The experimentally measured density matrix exhibits skyrmion textures as shown in the Figure S1(d)-(f), demonstrating clear topological characteristics in the spin configuration. Upon accurately obtaining the quantum Stokes parameters, the skyrmion number of the quantum skyrmion can be determined.

III. SIMULATION OF ATMOSPHERIC TURBULENCE

In our experimental framework, we model atmospheric turbulence as refractive index fluctuations induced by microscopic temperature and pressure variations. These perturbations initially manifest as phase fluctuations that evolve into compound phase-amplitude modulations during optical propagation. Our implementation employs the thin phase screen approximation, where the turbulence strength ischaracterized by the dimensionless ratio $\Omega = 2w/r_0$, with w representing the second moment beam waist and r_0 denoting Fried's atmospheric coherence length parameter, given by [4, 5]:

$$r_0 = 0.185 \left(\frac{\lambda}{C_n^2 z} \right)^{3/5}, \tag{S.12}$$

where C_n^2 is the refractive index structure constant, λ is the wavelength and z is the channel length. The strength of turbulent media can be quantitatively characterized by the Strehl ratio (SR). Under the single phase-screen approximation model, its mathematical expression is given by:

$$\mathrm{SR} \cong \frac{1}{\left[1 + (2w/r_0)\right]^{5/3}}. \tag{S.13}$$

Given the stochastic nature of atmospheric refractive index fluctuations, a statistical description is essential. In this study, we adopt two approaches. Due to its computational efficiency, we made use of a spatial frequency domain approach for the quantum measurements. This approach makes use of fast Fourier transforms (FFTs) to generate random spectral components based on a prescribed power-law spectrum. The methodology centers on implementing the Fourier transform of the refractive index covariance function. In the Fourier domain, the power spectral density of refractive index fluctuations is expressed as:

$$\Phi_n(\kappa) = 0.0033 C_n^2 k^{-11/3}. \tag{S.14}$$

This formulation represents the renowned Kolmogorov power spectral density model, where k denotes the spatial frequency. The power spectral density function provides the fundamental basis for optimally simulating atmospheric turbulence effects through stochastic sampling of spatial frequency components. The implementation involves generating turbulence phase screens via Fourier-domain synthesis, achieved by encoding the Fourier transform of the product between the power spectrum and a complex random field.

The phase screens corresponding to different turbulence strengths are presented in Figure S2(a)-(c). In our experimental setup, we employ a spatial light modulator to perform projective measurements on photon A, which necessitates the implementation of a composite grating incorporating three distinct components: (i) vortex phase grating, (ii) blazed grating, and (iii) turbulence-modulated grating, as schematically illustrated in Figure S2(d)-(g).

The classical simulations and experiments made use of Noll phase screens. The spectral domain is popular due to its computational efficiency achieved by leveraging optimized FFT algorithms. However, this approach is known to overestimate the high frequency spatial contributions and underestimate the low frequency components of turbulence [6]. This results in high frequency intensity perturbations in the propagation of optical beams leading to higher noise and falsely increases the number of phase and polarization singularities that are detected. In contrast, the Noll phase screens make use of Zernike which form a complete and orthogonal set of the unit disk and are commonly used in simulated and real world adaptive optics applications to correct for the wavefront aberrations induce by atmopsheric turbulence. They are given analytically by, The analytical form for the Zernike polynomials is therefore given as follows [7],

$$\left.\begin{aligned} Z_{\text{even j}}(r,\theta) &= \sqrt{n+1}\, R_n^m(r)\sqrt{2}\cos(m\theta) \\ Z_{\text{odd j}}(r,\theta) &= \sqrt{n+1}\, R_n^m(r)\sqrt{2}\sin(m\theta) \end{aligned}\right\} \quad m \neq 0\,, \\ Z_{\text{j}}(r,\theta) = \sqrt{n+1}\, R_0^m(r)\,, \qquad m = 0\,, \tag{S.15}$$

where r is the radial coordinate and θ is the azimuthal coordinate. The radial component is given by,

$$R_n^m(r) = \sum_{s=0}^{(n-m)/2} \frac{(-1)^s (n-s)!}{s![(n+m)/2-s]![(n-m)/2-s]!} \tag{S.16}$$

The polynomials have a known covariance in Kolmogorov turbulence [8, 9], which can be used to randomly sample weighting coefficients to build phase screens that statistically replicate the effects of atmospheric turbulence. Such an approach is computationally slower but shows better agreement with theoretical predictions of the Kolmogorov model. Full details in the implementation of this method can be found in Ref. [10].

IV. CALCULATION OF SKYRMION NUMBER FROM EXPERIMENTAL DATA

Contour integral calculation of the skyrmion number. Typical approaches to calculating the wrapping number of given field involve directly computing the surface integral. Due to the severe distortions induced by atmospheric turbulence on the beams' intensity profile, we made used of an alternative approach initially proposed by McWilliam *et al.* [11]. This approach involves using a contour integral to reframe the computation as follows,

$$N = \frac{1}{2} \left(\sum_j S_z^{(j)} N_j - S_Z^{\infty} N_\infty \right), \tag{S.17}$$

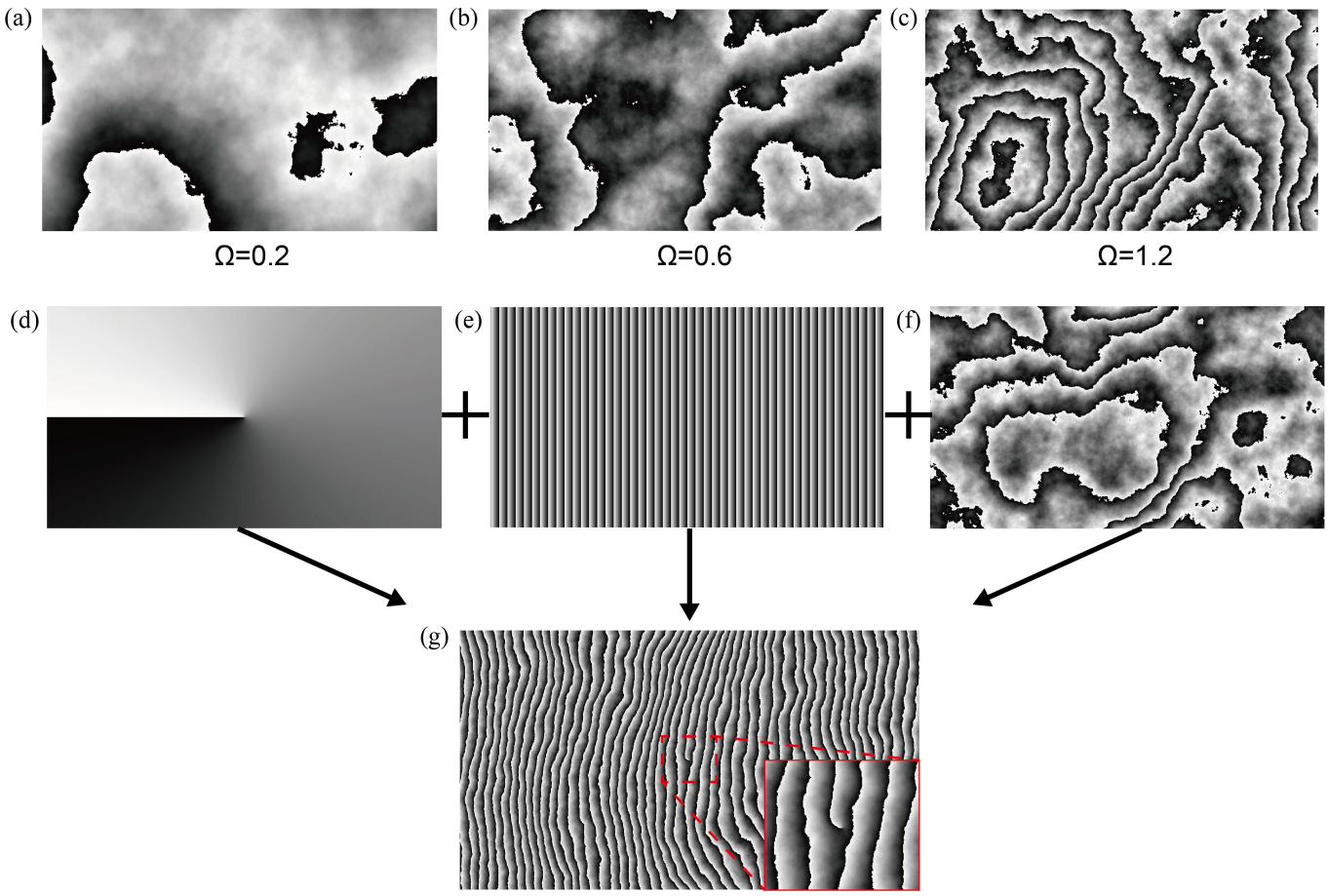

FIG. S2: **Grating configurations.** (a)-(c) respectively display dynamic grating diffraction patterns under three turbulence regimes: weak ($\Omega = 0.2$), moderate ($\Omega = 0.6$), and strong ($\Omega = 1.2$). (d) shows a vortex phase grating with topological charge $l = 1$. (e) presents a blazed grating. (f) display grating patterns with ($\Omega = 1.0$). (g) depicts the composite grating pattern (1920×1080 pixels) ultimately loaded onto the spatial light modulator.

where N_j is the charge of individual phase singularity at position j in the field $S_x + iS_y$, $S_z^{(j)}$ is the value of the Stokes parameter S_z at the point j, N_∞ is the result of the contour integral at infinity and $S_z^{(\infty)}$ is the value of the Stokes parameter S_z as $r \to \infty$. Any of the Stokes parameters (S_1, S_2 and S_3) can take the place of S_z, with the other two ordered taking the place of S_x and S_y.

Classical and quantum stokes parameters. In order to make use of Equation S.17, the Stokes parameters must be determined from experimental measurements. In the case of quantum skyrmions, the Stokes parameters are simply the observables of the Pauli matrices which can be calculate from the experimentally reconstructed density matrix $\sigma_{B,j}$ as follows,.

$$S_j = \langle | \overrightarrow{r_A} \rangle \langle \overrightarrow{r_A} | \otimes \sigma_{B,j} \rangle = \left\langle \Psi_{B|A} \right| \sigma_{B,j} \left| \Psi_{B|A} \right\rangle . \quad \text{(S.18)}$$

Classical Stokes parameters are obtained through traditional Stokes polarimetry using six experimentally measured polarization intensity projections,

$$s_0 = I_H + I_V \quad \text{(S.19)}$$
$$s_1 = I_H - I_V \quad \text{(S.20)}$$
$$s_2 = I_D - I_A \quad \text{(S.21)}$$
$$s_3 = I_R - I_L . \quad \text{(S.22)}$$

The subscripts H, V, D, A, R and L represent horizontal, vertical, diagonal, antidiagonal, right circular and left circular polarizations respectively. A polarization sensitive camera was able to measure the four linear polarization intensity projections. A quarter-wave plate was placed in from the of the camera in order to measure the circular intensity projections [12]. Equation S.17 requires the locally normalized Stokes parameters S_j which were computed from the experimentally obtained Stokes parameters s_j according to,

$$S_j = \frac{s_j}{\sqrt{s_1^2 + s_2^2 + s_3^2}} \quad \text{(S.23)}$$

Polarization singularities. The contour integral can be taken over one of three polarization fields,

$$P_1 = S_2 + iS_3 \quad \text{(S.24)}$$
$$P_2 = S_3 + iS_1 \quad \text{(S.25)}$$
$$P_3 = S_1 + iS_2\,. \quad \text{(S.26)}$$

While all three are theoretically equivalent, numerical and practical considerations may cause one choice to perform far more reliably than others. In this work. P_1 exhibited erratic behaviour over various realizations as compared to P_2 and P_3 and so was excluded. Once the polarization field were obtained, the positions and charges of the phase singularities of these fields were determined using a numerical equivalent to the curl $\nabla\times$ operation (first proposed in Ref [13]) termed the circulation D. The circulation is defined as,

$$\begin{aligned} D^{m,n} = \tfrac{d}{2}\ & (G_x^{m,n} + G_x^{m,n+1} + G_y^{m,n+1} + G_y^{m+1,n+1} \\ & - G_x^{m+1,n+1} - G_x^{m+1,n} - G_y^{m+1,n} \\ & - G_y^{m,n})\,. \end{aligned} \quad \text{(S.27)}$$

Here, $D^{m,n}$ represents the value of the circulation of the pixel in the n-th row and m-th column. $G_x^{m,n}$ and $G_y^{m,n}$ are the phase gradient in the horizontal and vertical direction of the pixel in the n-th row and m-th column, respectively and d is the pixel size. Typically, the circulation will return a 0 value if there is no singularity at that pixel and a nonzero value if there is. The magnitude of the circulation indicates the charge of the singularity and the sign indicates the direction/handedness of the singularity. These values were then substituted into Equation S.17 to calculate N.

V. POST-PROCESSING OF CLASSICAL EXPERIMENTAL DATA

The local normalization of the Stokes parameters in Equation S.23 is necessary to ensure the accurate calculation of the wrapping number. However, it also results in the amplification of random noise in low intensity regions of experimental data. This noise can be caused by ambient environmental light and the shot noise of the detector. If it is not considered or filtered off, it will artificially increase the number of polarization states present the measurement and result in an inaccurate determination of the skyrmion number. We therefore implemented a standard post-processing procedure following the one outlined in the supplementary of Ref. [14] that was calibrated on unaberrated beams for each of the configurations tested: near-field, far-field and single phase screen propagation. The parameters in each case were kept constant irregardless of the turbulence strength or incident N, ensuring the measurement system and procedure was agnostic of the specific topology or turbulence strength.

For the near-field results, an intensity based threshold was implemented. The singularities of the polarization field was calculated, and any singularity found in regions where the measured intensity was below the noise floor were disregarded. To determine the noise floor, regions near the edges of the captured CCD images, far removed from the generated beam, were isolated and the intensity values averaged. The average noise value over multiple measurements was found to be $\approx 3\%$ of the maximum intensity. Therefore, any singularity detected in regions with intensities lower than 3% of the maximum beam signal were disregarded from the calculation of the skyrmion number. This was kept constant for all of the near-field measurements. The far-field measurements implemented the same intensity based threshold and also included a low-pass 2D Gaussian filter with kernel of standard deviation $\sigma = 1220$ m^{-1}. The far-field saw the manifestation of the high frequency intensity features due to the propagation of the light. These high frequency intensity features result in additional singularities which affect the wrapping number calculation, thus necessitating the need for the Gaussian filter. The kernel size and threshold were kept constant for all of the far-field measurements. The propagation results made use of an intensity threshold of 3% and Gaussian filter with kernel $\sigma = 732$ m^{-1} which again was kept constant for all of the propagation measurements.

VI. PARAMETERS FOR MULTIPLE PHASE SCREEN SIMULATIONS

The multiple phase screen simulations were performed in MATLAB. We made use of an initial grid size of 1024×1024 pixels with pixel size $\delta x = 160$ μm. The maximum radius of the Zernike polynomials was set to $R_{max} = 82$ mm and 128 Zernike modes were used in the construction of the turbulence phase screens. The skyrmions were generated through vectorial combinations of LG beams, with the embedded Gaussian beam waist $w_0 = 25$ mm. The length of the channel was $L = 1$ km with a spacing of $\Delta z = 200$ m between the five screens. Channels with Rytov variances $\sigma_R^2 = 1.0$, 1.5, 2.0, 2.5 and 3.0 were tested, with corresponding Fried parameters for each unit cell being $r_{0,s} = 50, 39, 33, 29$ and 26 mm respectively and thus total channel Fried parameters of $r_0 = 19.0$, 14.9, 12.6, 11.0 and 9.85 mm respectively. Each simulation saw 100 independent, random realizations for each of the five phase screens.

[1] Z. Guo, Z. Chang, Y. Zhang, G. Ma, X. Zhu, J. Jia, and P. Zhang, Opt. Express **31**, 7632 (2023).

[2] M. S. Kaznady and D. F. James, Phys. Rev. A **79**, 022109 (2009).

[3] P. Ornelas, I. Nape, R. de Mello Koch, and A. Forbes, Nat. Photon. **18**, 258 (2024).
[4] D. L. Fried, JOSA **56**, 1372 (1966).
[5] B. Ndagano, B. Perez-Garcia, F. S. Roux, M. McLaren, C. Rosales-Guzman, Y. Zhang, O. Mouane, R. I. Hernandez-Aranda, T. Konrad, and A. Forbes, Nature Phys **13**, 397 (2017).
[6] D. Bachmann, M. Isoard, V. Shatokhin, G. Sorelli, and A. Buchleitner, Optical Engineering **64**, 058102 (2025).
[7] M. Born and E. Wolf, *Principles of optics: electromagnetic theory of propagation, interference and diffraction of light* (Elsevier, 2013).
[8] R. J. Noll, Journal of the Optical Society of America **66**, 207 (1976).
[9] N. A. Roddier, Optical engineering **29**, 1174 (1990).
[10] C. Peters, V. Cocotos, and A. Forbes, Advances in Optics and Photonics **17**, 113 (2025).
[11] A. McWilliam, C. M. Cisowski, Z. Ye, F. C. Speirits, J. B. Götte, S. M. Barnett, and S. Franke-Arnold, Laser & Photonics Reviews **17**, 2300155 (2023).
[12] M. A. Cox and C. Rosales-Guzmán, Applied Optics **62**, 7828 (2023).
[13] M. Chen, F. S. Roux, and J. C. Olivier, Journal of the Optical Society of America A **24**, 1994 (2007).
[14] C. Peters, K. Everts, T. Kleine, P. Ornelas, and A. Forbes, arXiv preprint arXiv:2508.12305 (2025).